water

MDPI

Article

Self-Regenerating Solar Evaporation System for Simultaneous Salt Collection and Freshwater from Seawater

Muneerah Alomar [1,*], Badriah S. Almutairi [1], Seham S. Alterary [2], Manal A. Awad [2], Fida Hussain [3], Awatif A. Hendi [1], Maha F. El-Tohamy [2] and N. Al-Hoshani [4]

[1] Department of Physics, College of Science, Princess Nourah bint Abdulrahman University, P.O. Box 84428, Riyadh 11671, Saudi Arabia; bsalmutairi@pnu.edu.sa (B.S.A.)
[2] Department of Chemistry, College of Science, King Saud University, P.O. Box 11495, Riyadh 11362, Saudi Arabia
[3] Department of Chemical and Energy Engineering, Pak-Austria Fachhochschule, Institute of Applied Science & Technology, P.O. Box 22620, Haripur 22652, Khyber Pakhtunkhwa, Pakistan; fidaya@gmail.com
[4] Department of Biology, College of Science, Princess Nourah bint Abdulrahman University, P.O. Box 84428, Riyadh 11671, Saudi Arabia
* Correspondence: muaalomar@pnu.edu.sa; Tel.: +966-509811261

Abstract: Water scarcity is a serious issue which is increasing gradually due to rapid industrialization and population explosion. Biomass-inspired photothermal materials are of great importance due to their low-cost and enhanced photothermal conversion efficiencies. Herein, a pyrolyzed honokiol biochar (HB) is successfully synthesized to fabricate a self-regenerating solar evaporating system for in situ freshwater, and salt collection from seawater. The pyrolyzed biochar was innovatively printed onto a non-woven fabric (HB@NF) that exhibits excellent solar absorption (96%), and efficient stability in seawater. The self-regenerating structure is constructed in two parts: (1) HB-printed fabric as a photothermal layer for efficient solar-to-vapor conversion efficiencies (93%) under 1 kW m^{-2}. (2) Umbrella-like centralized seawater supply via cigarette filter to achieve the Marangoni effect for in situ water evaporation and salt collection. More importantly, effective thermal management achieved efficient heat accumulation (48.5 °C) under one sun intensity (1 kWm^{-2}), and its validation is also demonstrated in a COMSOL heat transfer simulation. Furthermore, a series of experiments on salt collection over different periods, evaporation stability under different cycles, and rejection of primary metal ions via Inductively Coupled Plasma–Optical Emission Spectrometry (ICP–OES) have been investigated. It is believed that this work will create new avenues regarding in situ freshwater and minerals recovery from seawater.

Keywords: water scarcity; solar evaporation; honokiol; self-regeneration; freshwater; salt collection

Citation: Alomar, M.; Almutairi, B.S.; Alterary, S.S.; Awad, M.A.; Hussain, F.; Hendi, A.A.; El-Tohamy, M.F.; Al-Hoshani, N. Self-Regenerating Solar Evaporation System for Simultaneous Salt Collection and Freshwater from Seawater. *Water* **2023**, *15*, 3697. https://doi.org/10.3390/w15203697

Academic Editors: Andreas Angelakis and Anas Ghadouani

Received: 12 August 2023
Revised: 20 September 2023
Accepted: 16 October 2023
Published: 23 October 2023

1. Introduction

Freshwater supply and population growth are two of the most pressing problems of the 21st century. By 2025, it is predicted that there will be an additional 3.9 billion people coping with water scarcity [1,2]. Thus, research into effective freshwater resource development strategies is of paramount importance. Through the use of solar–thermal technology, solar energy can be used to produce at large scales, including desalination, wastewater treatment, and water purification [3–5]. Solar-powered interfacial evaporation systems that effectively absorb solar light over the whole solar spectrum and employ superior thermal management may offer a promising solution to water shortage [6]. The efficient conversion of solar energy into steam is a key feature of the best solar steam generating system. In addition, it must have superior stability, scalability, optimal thermal management with minimum thermal losses, salt resistance, and a simple infrastructure for practical implacability. (1) Studies have been conducted on the photothermal properties of semiconductors [7], carbon-based materials [8–10], plasmonic metallic

nanoparticles [11], and conjugated polymers [12–14]. A common problem with the solar absorbers that have been developed is low energy-conversion efficiency, i.e., low solar absorption, salt accumulation, poor thermal management, and ultimately low freshwater yield [15]. (2) Evaporators with traditional two-dimensional (2D) planar structures are theoretically at the limit of energy efficiency. As a result of the planar structure, they tend to reflect more light, radiate more heat, and lose more energy through thermal convection. Several researchers have synthesized three-dimensional (3D) macrostructures, such as origami tessellations, conical shapes, self-contained monolithic sponges, origami roses, cylindrical structures, and 3D printed frameworks to maximize the capturing of solar light and ultimately the efficiency of the overall system by facilitating multiple reflections and minimizing energy loss [16–19]. Solvents exert osmotic pressure when moving through semi-permeable membranes to equalize solute concentrations on both sides [9]. A negative osmotic pressure gradient indicates lower solute concentrations in the upper solution than in the lower solution [9]. Water moves from areas of low solute concentration to areas of higher solute concentration when transported from the water body to its surface [9]. This analogy can help illustrate the driving force behind fluid ascent in different contexts, including biological processes.

Biochar is primarily produced from biomass that undergoes thermochemical conversion processes such as pyrolysis and gasification to yield biofuels. The utilization of biofuels is commonly denoted by the term Negative Emission Technologies (NET) due to the fact that the release of CO_2 is typically assimilated by photosynthesis and subsequently reabsorbed from the atmosphere [20,21]. Biochar can be employed as an adsorbent to remove various contaminants from water and wastewater i.e., volatile organic compounds, heavy metal ions, pesticides, pharmaceuticals, dyes, and polycyclic aromatic hydrocarbons [22]. In the world of bi-phenols, Honokiol belongs to a class called neo-lignans [23]. Despite being a polyphenol, it is relatively small and interacts with cell membrane proteins through intermolecular interactions. Among these are hydrogen bonds, hydrophobic interactions, and aromatic covalent interactions [24,25]. Typically, hydrophobic biochar is employed as a solar absorber in a bilayer floating structure with low density and conductivity, attached to a hydrophilic structure that serves as a channel for carrying water. In this context, Irshad et al. also reported the safe use of biochar bio-polluted plants as photothermal material in a hybrid solar-driven evaporation system for in situ water–electricity–salt generation, which also reduces the pressure on the environment to reach carbon neutrality [20]. Biomass photothermal materials offer the most effective choice for hybrid solar evaporators exhibiting efficient light-to-heat conversion at an affordable price and being abundant in nature [26–29]. This opens up new opportunities for biomass applications in solar-driven steam generation, especially in solar-triggered salt collection applications.

Herein, pyrolyzed honokiol biochar (HB) is successfully synthesized to fabricate a self-regenerating solar evaporating system for in situ freshwater and salt collection from seawater. The pyrolyzed biochar was innovatively printed onto a non-woven fabric (HB@NF) that exhibits excellent solar absorption (96%), and efficient stability in seawater. The self-regenerating structure is constructed in two parts: (1) HB-printed fabric as a photothermal layer for efficient solar-to-vapor conversion efficiencies (93%) under 1 kW m^{-2}. (2) Umbrella-like centralized seawater supply via cigarette filter to achieve the Marangoni effect for in situ water evaporation and salt collection. HB-printed fabric is characterized by its heterogeneous diffuse morphology, which permits it to absorb solar radiation omnidirectionally (96%) and remain chemically stable in water and seawater, whereas the centralized water channels ensure efficient and balanced water transportation to maximize solar evaporation, along with salt edging for salt harvesting. An open porous microstructure and hydrophilic ultra-long nodes are characteristic of the periodic array structure of HB-printed fabric (HB@NF). Consequently, the surface temperature of the fabric (49.4 °C) is enhanced due to multiple scattering and reduced thermal conductivity (0.26481 ± 0.02948 Wm^{-1} K^{-1}). Additionally, under one sun illumination (1 kWm^{-2}), water vaporizes at a rate of 1.64 kg m^{-2} h^{-1}. As a result, an enhanced solar-to-vapor

conversion efficiency of 84% is achieved. The presented work opens up new opportunities for developing a self-regenerating system that facilitates the occurrence of two mechanisms (photothermal and Marangoni effect) driven by solar energy for the production of fresh water and salt collection, as illustrated in Figure 1. The detailed experimental setup, especially the controlled solar-driven evaporation setup, is explained in Supplementary Information Note S1.

Figure 1. Illustration of a solar evaporation system for simultaneous salt and freshwater production.

2. Materials and Methods

Honokiol powder was offered by FocusHerb LLC Co., Ltd. (Xi'an, China) Polystyrene foam (PSF), smoke filter, and non-woven fabric were purchased from Wuhan Guangfu fine synthetic industry, while K-6325 UV-glue was offered by Aladdin Chemical Reagent Co., Ltd. (Shanghai, China) All the materials were purified up to 99% and directly processed without any additional purifying treatments.

2.1. Synthesis of Honokiol Biochar (HB)

First of all, the dried powder of honokiol-rich leaves was subjected to heating in the presence of a nitrogen atmosphere within a tube furnace by placing it inside a ceramic crucible. The honokiol powder was heated by adjusting to 15 °C min^{-1} (the heating rate was adjusted for a maximum of 15 °C temperature increase per minute with a maximum increase of temperature up to 400 °C for 2 h followed by a 2 h period of free cooling). To remove any remaining bio-oil adhering to the biochar surface, the resulting honokiol biochar (HB) powder was sieved through a 80 mesh strainer (0.17 mm) and stirred constantly with cyclohexane solution (1:40 w/v) overnight. Cyclohexane is a cycloalkane hydrocarbon that is used as a solvent to extract certain compounds or impurities from biochar produced during pyrolysis. Afterward, the sand core funnel underwent multiple rounds of suction filtration of the resulting powder using ethanol, unless the obtained filtrate achieved clarity. Finally, the obtained honokiol biochar was placed on the filter cake and heated in the oven for 4 h at 80 °C, resulting in the production of the ultimate black powder of honokiol biochar which was saved for the photothermal experiment.

2.2. HB-Printed Fabric

The ultra-black honokiol biochar (HB) was innovatively coated onto a non-woven fabric for the fabrication of self-regenerating solar evaporating systems, as demonstrated in Figure 2. For this, the UV-dried printing technique was employed for sustainable and stronger deposition. In the first step, prepared HB powder (1.5 g) was dissolved into a hydrophilic UV glue (K-6325). The black slurry was evenly coated onto a crafted non-woven fabric by paintbrush and dried under UV-365 nm irradiations (2 h). In general, non-woven fabric is regarded as a textile-like substance that is produced by combining long fibers (continuous in length) and staple fibers (short in length) using mechanical, chemical, solvent, or thermal processes to form a cohesive structure. Threads are often composed of natural fibers, such as cotton or wool. Afterward, the HB-printed fabric was selected as an interfacial heating layer for photothermal steam generation whereas the hydrophilic cigarette filter reinforced with capillary action was adopted as a centralized water supply path for water transportation, while the photothermal layer is supported by self-floatable, and hydrophobic polystyrene foam (PSF) which is also utilized for the self-standing and salt collection stage. The selection of PSF ensures the self-floating potential and good thermal insulation to reduce the heat losses of the overall system. Furthermore, the experimental setup of evaporation performances and COMSOL Multiphysics heat transfer simulation calculations are provided in Supplementary Information Notes S1 and S2.

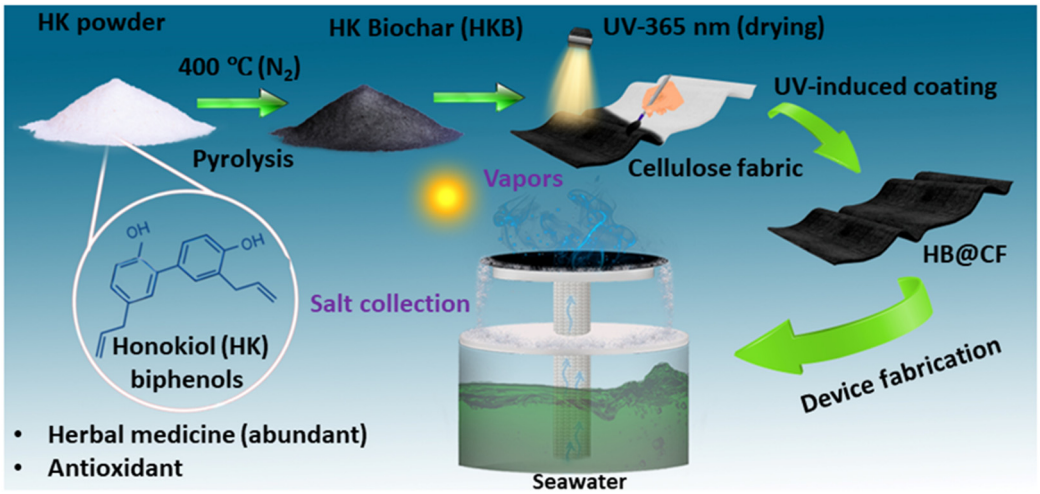

Figure 2. Synthesis of honokiol biochar (HB), UV-induced printing, and device fabrication for in situ freshwater and salt collection from seawater.

2.3. Results & Discussion

The surface elemental composition, chemical states, and surface functional groups of the pyrolyzed honokiol biochar (HB) were analyzed by performing X-ray photoelectron spectroscopy (XPS) and Fourier transform infrared spectroscopy (FTIR). The XPS spectra of HB (Figure 3a) consist of three characteristic peaks positioned at 284.26, 398.60, and 533.31 eV, revealing the existence of C1s, N1s, and O1s as a major component, which is primarily attributed to the carbohydrates and peptide bonds in the proteins of HB [23–25]. The high-resolution XPS spectrum of carbon (C1s) shows three sub-peaks located at 284.39 eV, 285.16 eV, and 288.47 eV owing to the presence of two C-C, C-N/C-O, and C=O bonds (Figure 3b). Normally, biochar obtained from grass and leaves contains high nitrogen content compared to feedstock's biochar, i.e., wood, due to the presence of high protein. The highly resolved XPS spectrum of N1s is shown in Figure 3c, which is deconvoluted into five sub-peaks located at 398.63, 398.87, 398.98, 399.44, and 400.12 eV binding energies, revealing the presence of C-N/N-H, pyrrolic-N, and pyridinic-N bonds, respectively [23], whereas the O1s spectrum is decomposed into four sub-peaks showing the existence of various oxygen-containing groups such as double-bounded oxygen with carbon in carbonyl

(C=O), single-bonded oxygen with carbon in aromatic rings and phenols (C-O, C-O-C) and hydroxyl groups (O-H) located at 530.34, 531.89, 532.72, and 532.70 eV, as shown in Figure 3d. The surface functionality of the honokiol biochar nanoparticles (NPs) was determined by carrying out FTIR spectroscopy, as demonstrated in Figure 3e.

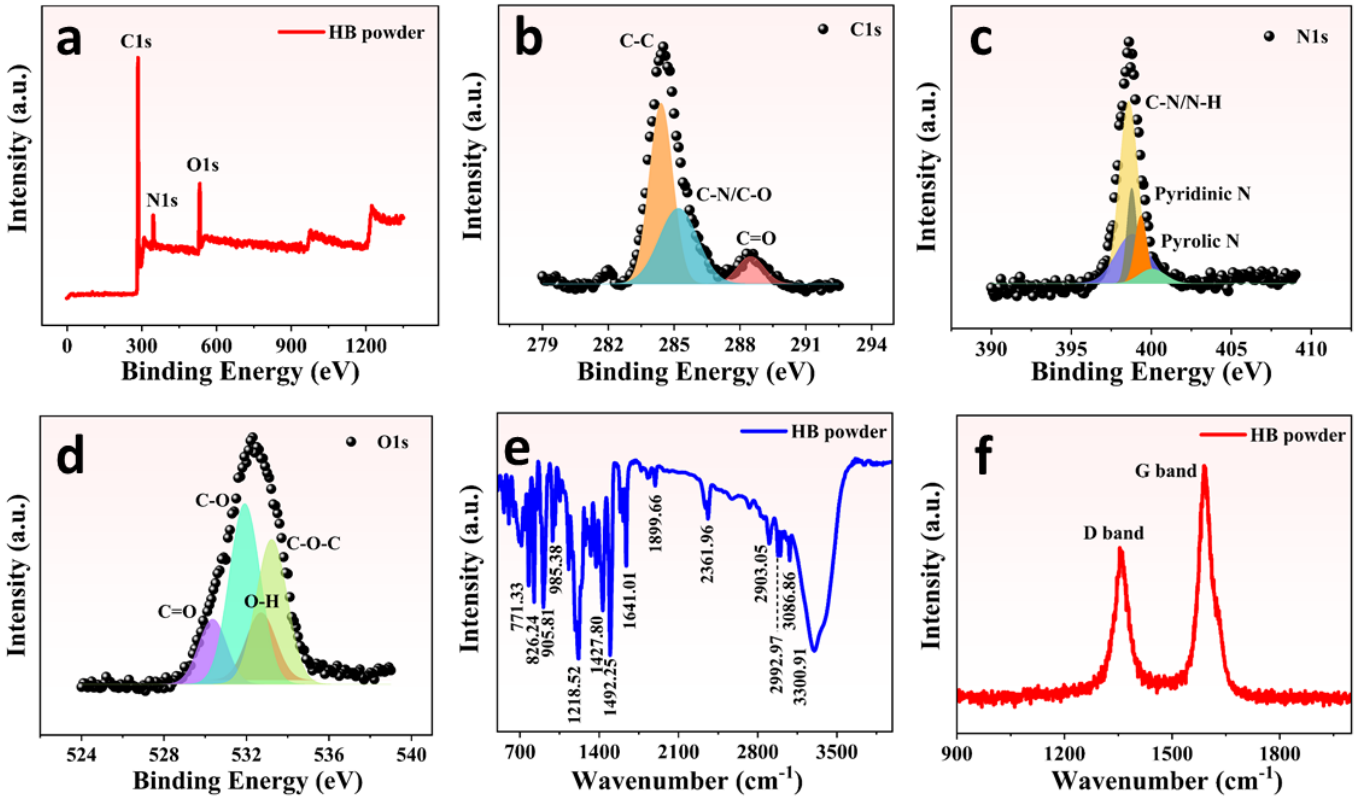

Figure 3. (**a**) XPS spectra of honokiol biochar. (**b**–**d**) C1s, N1s and O1s spectrums. (**e**) FTIR spectrum of HB NPs. (**f**) Raman spectrum of HB NPs.

The absorption peaks from 700–900 cm^{-1} correspond to N-H bending, whereas peaks from 900–1200 cm^{-1} are due to the C-O stretching peaks of aromatic rings. The bands appearing from 1200–1600 cm^{-1} are mainly due to the symmetric vibrations of C=O from COO- groups and C-N groups. The absorption bands observed in honokiol biochar within the range 1600–3000 cm^{-1} can be ascribed to the out-of-plane stretching of aromatic C=C and C-H. The bands appearing from 3000 to 3400 cm^{-1} correspond to the vibrations of the O-H bond in the hydroxyl groups [23]. The FTIR results were in good agreement with the XPS findings, which showed that the pyrolyzed honokiol biochar has various hydrophilic bonds, such as C-O, C-O, and N-H, which promote the transportation and distribution of water. Further, the structural features of the honokiol biochar were analyzed by performing Raman spectroscopy, as shown in Figure 3f. The Raman spectra of HB show the two characteristic bands at 1355.19 cm^{-1} (D band) and 1590.19 cm^{-1} (G band). The G band is mainly due to the vibrating modes of the sp2-hybridized carbon atom in graphitic carbon, while the D band is related to the disordered structures of carbon.

An analysis of the microstructure and surface morphology of pyrolyzed honokiol biochar (HB) powder and HB-printed non-woven fabric (HB@NF) was performed by Field Emission Scanning Electron Microscopy (FESEM). The surface morphology of pyrolyzed honokiol biochar (HB) reveals that the majority of particles are rod-like microstructure, as illustrated in Figure 4a–d. Figure 4e,f shows that the HB particles are uniformly deposited on the hydrophilic nodes of the non-woven fabric, that the texture remains rough and decorated with rod-like HB particles, and that the porous surface ensures efficient light absorption and water absorption. Non-woven fabrics in the field of textile engineering

are produced by the process of fiber entanglement, as opposed to conventional weaving techniques. Non-woven materials are used in solar-driven evaporation systems for water pumping purposes owing to their distinctive attributes, including their capillary action. Capillary action refers to the phenomenon in which a liquid can flow through small gaps or porous materials, defying the pull of gravity. The fibrous nature of non-woven textiles renders them very conducive to water absorption and retention. The capillary action facilitates the upward movement of water through the interstitial gaps between fibers when a non-woven fabric is immersed in water at one end. The presence of gaps is responsible for the phenomenon of capillary action in water. The capillary-driven mechanism obviates the need for external energy sources in the solar-driven evaporation system, such as mechanical pumps. The use of eco-friendly and energy-efficient methods for freshwater production in distant regions serves as a viable solution to combat water shortage.

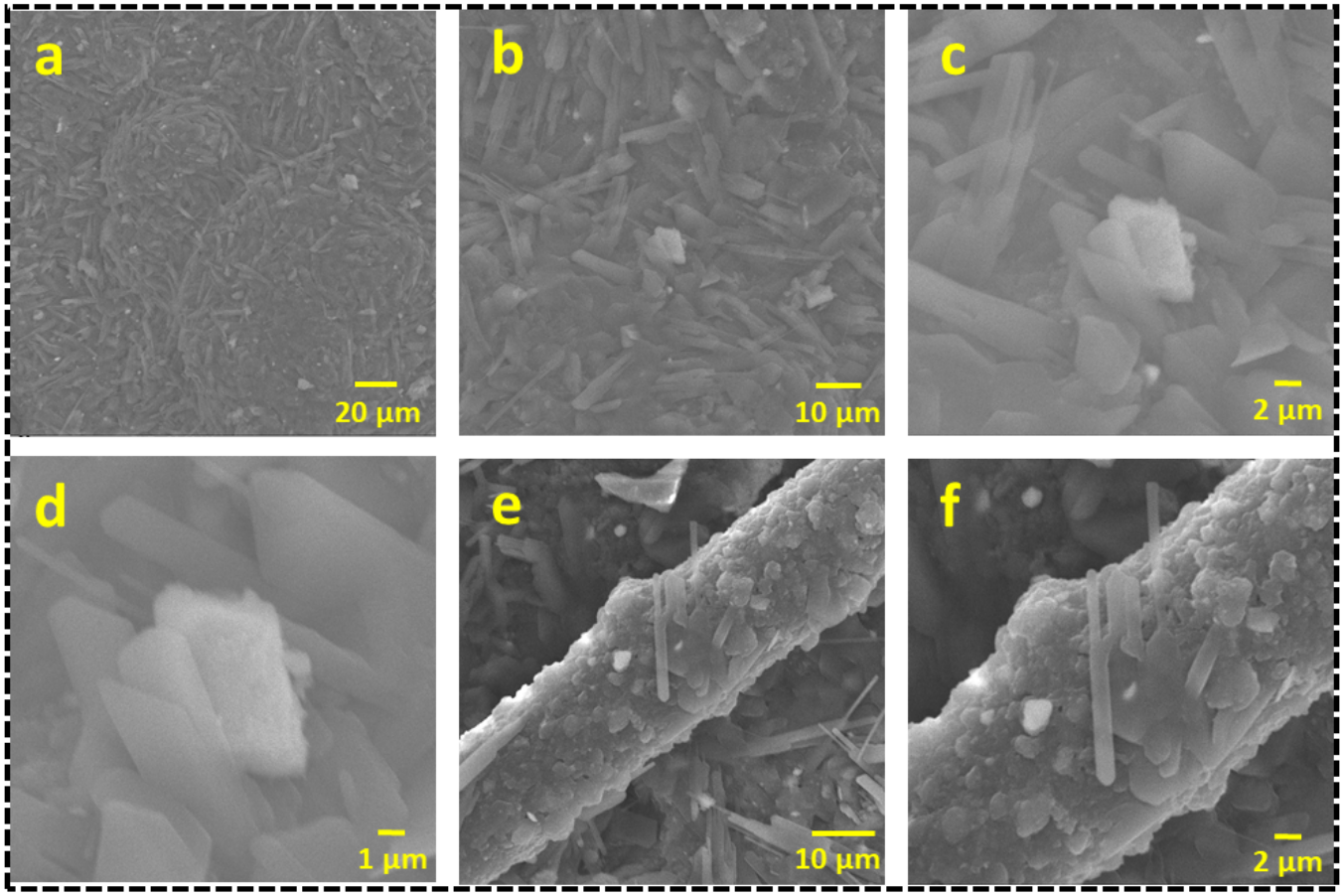

Figure 4. Microstructural and morphological analysis. FESEM images of (**a**–**d**) pyrolyzed honokiol biochar with different magnifications, and (**e**,**f**) UV-induced HB-printed non-woven fabric at different resolutions.

In Figure 5a, the solar absorption of pyrolyzed honokiol biochar was analyzed by performing UV–Vis spectroscopy. Based on UV spectra, ultra-black HB exhibits a significant enhancement in solar absorption (96%) (excluding reflection and transmission). This enhancement of solar absorption is attributed to its porous, rough, and non-uniform morphology, as well as the associated conjugated π bonds. The dense and dark top surface texture of the HB@NF hybrid evaporator effectively promotes the scattering of incoming light inside the surface, hence enriching its capacity for solar light absorption.

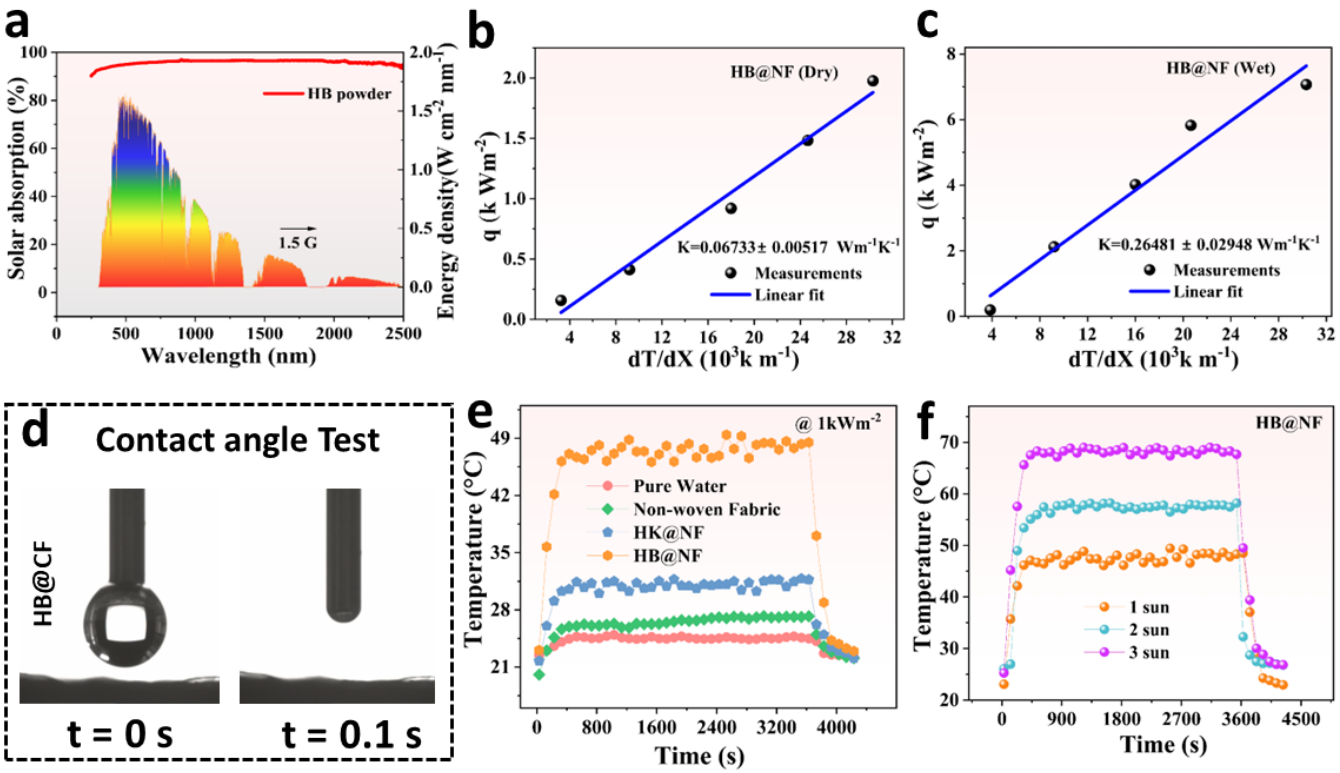

Figure 5. (**a**) UV–Vis spectrum of honokiol powder and honokiol biochar. (**b**,**c**) Thermal conductivity of wet HB@NF printed fabric. (**d**) Water contact test of HB@NF. (**e**,**f**) The enhanced surface temperature of UV-induced printed HB@NF fabric under different solar irradiation.

The total effectiveness of the steam generating system can be optimized with precise temperature regulation. An experimental thermal conductivity measurement was taken utilizing a thermal conductivity meter (Hot Disk, TPS 2500, Sweden hot disk collaboration) to determine the HB@NF hybrid evaporator's thermal conductivity. When the system is turned on, a temperature gradient is characterized by a continuous rise or fall in temperature (dT/dx) along the vertical axis. The use of Fourier analysis may be employed to comprehend the heat transfer rate (q) of the HB@NF hybrid evaporator [12]:

$$q = -k_1 \frac{dT}{dx} = -k_1 \frac{T_2 - T_1}{x_2 - x_1} \quad (1)$$

From the above, k_1 indicates the thermal conduction (1.05 W m^{-1}K^{-1}), x_1 denotes the glass width (3 mm) used to sandwich the system, and x_2 is the total height of HB@NF (30 mm), where T_1 represents the temperature measurement of the thermal conductivity measuring device, T_2 corresponds to the bottom and T_3 to the top surface temperature recording of the HB@NF hybrid evaporator. Using the following equation, the thermal conductivity (k) of the system was determined at an equilibrium level of temperature maintenance rate [12]:

$$k = q \frac{x_2}{T_3 - T_2} \quad (2)$$

From the above experiments, HB@NF exhibits a notably low thermal conductivity of 0.06733 ± 0.00517 Wm^{-1} K^{-1}. This is primarily attributed to the phenomenon of multiple scattering, which occurs when incident light is redirected toward the interior of the interfacial surface. As a result, the energy carried by the light is converted into heat and transferred to the photothermal surface. Additionally, this system effectively maintains a minimal thermal conductivity flow towards the downward structure of the overall system. The elevation of interfacial layer temperature, in conjunction with little thermal conduction, plays a crucial role in achieving effective thermal management (Figure 5b). The thermal

conductivity of wet HB@CF was also measured (Figure 5c), and wet HB-printed fabric is approximately two times less thermally conductive than water (0.6 $Wm^{-1}K^{-1}$).

It is beneficial to take advantage of efficient solar absorption and minimal thermal conduction to maximize the accumulation of interfacial heat and improve the efficiency of solar-to-vapor conversion. The water contact angle of HB@NF is shown in Figure 5d, which indicates that its open porous microstructure validates its hydrophilicity. Any built solar energy-based system's ability to capture solar light and convert it into heat with the least amount of thermal conduction to bulk water is crucial to obtain high efficiency. The hybrid HB@NF hybrid solar evaporator demonstrates exceptional solar absorption capabilities as well as effective conversion of solar energy into thermal energy, while also effectively limiting thermal passage to the lower matrix. In this study, measurements were conducted on the surface temperatures of four different systems: pure water, non-woven fabric (NF), honokiol powder @NF (HK@NF), and honokiol biochar@NF (HB@NF), to comparatively asses the flux distribution potential of these systems. For this, the interfacial temperature enhancements of each system were recorded under a heat flux of 1 kWm^{-2} for a duration of 1 h. Two thermocouples were used to measure the temperatures, and they were positioned in the designated regions, as shown in Figure 5e. The HB@NF hybrid evaporator demonstrates optimal solar energy capture, effective distribution of heat flux across the upper matrix, and efficient thermal management that restricts heat conduction downwards while facilitating water conduction towards the top surface. Consequently, the interfacial photothermal surface exhibits a quick temperature rise, reaching about 49.4 °C, and eventually attains an equilibrium temperature for the upper surface of HB@NF, demonstrating a remarkable photothermal conversion efficiency. The achievement of a high surface temperature facilitates rapid steam production, eventually resulting in enhanced efficiency. Measurements of HB@NF's surface temperature were also taken at a variety of simulated solar irradiances, with the highest value reaching 68.9 °C at 3 kWm^{-2} (Figure 5f).

Excellent thermal management depends on the enhancement of the interfacial surface temperature, as well as a minimum of thermal conduction. The infrared (IR) camera was used to identify the interfacial heat localization of the self-regenerating system from both a top surface and a cross-sectional view under one solar illumination, as illustrated in Figure 6a.

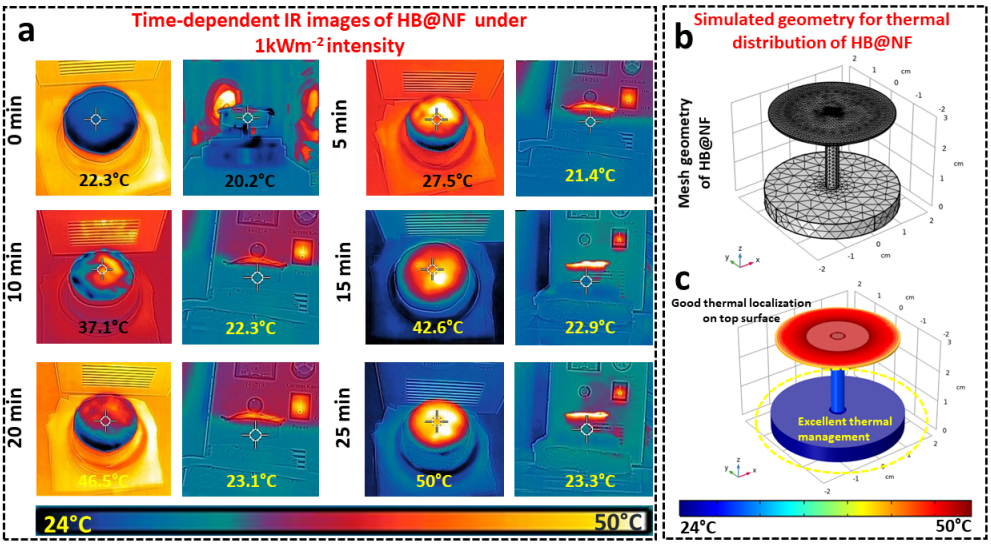

Figure 6. (**a**) Time-dependent IR images of HB@NF hybrid evaporator during solar evaporation showing thermal distribution for the top surface and excellent thermal insulation for the cross surface. (**b**,**c**) The mesh geometry and corresponding developed heat transfer model of the HB@NF hybrid evaporator using COMSOL Multiphysics software (version 6.1).

The temperature of HB@NF increases to 37.1 °C in 10 min due to the prompt photothermal transition, resulting in heat buildup on the upper surface. In this experiment, it was observed that the bottom structure of the HB@NF process consistently retained a temperature of 23 °C, which was significantly lower than its upper surface. This indicates that there was no heat conduction in the downward direction, and the top surface exhibited effective thermal insulation, resulting in optimal thermal localization. The HB@NF hybrid solar evaporator combines anisotropic low thermal conduction and efficient photothermal conversion to provide optimal "Thermal localization" and therefore a high rate of evaporation. The optimization of heat loss reduction plays a crucial role in enhancing the performance and efficiency of hybrid solar harvesting systems.

To speculate on the internal temperature distribution within the interfacial matrix, a heat transfer model using advanced COMSOL Multiphysics 5.5 was developed for the HB@NF hybrid evaporator by simulating the actual dimensions and extensive set of components to investigate the heat generation patterns and effect of thermal loads, e.g., properties of materials, water and surface temperature, and specific boundary conditions corresponding to the actual parametric dimensions. The developed simulated model exactly imitates the actual design and dimensions of IR images for the HB@NF hybrid evaporator, which are situated at the upper edge, acting as thermal insulation for the external boundaries. The negligible thermal conductivity of the downward matrix of the HB@NF hybrid evaporator creates a substantial temperature gradient across the interface, limiting how much heat may escape downwards through the mesh. Element shrink was modified by setting the element scale factor to 1, and the physics-controlled mesh with normal element size was chosen.

Figure 6b shows the mesh geometry of the HB@NF hybrid evaporator, divulging the attainment of excellent flux distribution over the interfacial surface with excellent thermal management due to minimum thermal conductivity, and ultimately an enhanced surface temperature (41.33 °C) is achieved. The growth rate swings towards tetrahedral mesh in the center and lower domains. Conversely, a rise in the number of mesh elements results in a reduction in the size of the interfacial layer and boundary elements. This leads to a higher resolution confined specifically to the interfacial and boundary surfaces. In areas of the mesh characterized by uniform element size, particularly when the flux distribution remains constant, the growth rate converges towards a maximum value of 1. It is smaller when the temperature gradient is higher, as shown by an increase in the growth rate of elements from one to the next. The confined water path via smoke filter provides exceptional thermal insulation at interfacial points due to the small contact area with the interfacial surface. The interfacial surface of the HB@NF hybrid evaporator exhibits good thermal divergence around insulating edges and an abrupt decrease in temperature is observed towards the lower matrix from the interfacial points, as depicted in Figure 6c. Simulation models were developed to contribute to greater accuracy in predicting the practical devices used for heat transfer. The thermal localization on the upper surface of the HB@NF hybrid evaporator plays a crucial role in enabling efficient photothermal conversion of solar radiation. This is achieved by effectively dispersing the incoming solar light at the interface, which serves as the fundamental process for generating solar steam there. In this study, four different evaporation systems were examined, including pure water, non-woven fabric (NF), HK@NF, and HB@NF, for continuous vapor production at an irradiation intensity of 1 kWm^{-2} for a duration of 1 h to compare and assess the evaporation rate and efficiency of these systems.

The good photothermal conversion coupled with good thermal management results in raised surface temperatures, hence facilitating greater evaporation and an increased rate of evaporation. The maximum recorded evaporation rate of 1.64 kg $m^{-2}h^{-1}$ is seen in the HB@NF system, surpassing other constructed systems, such as pure water (0.64 kg $m^{-2}h^{-1}$), non-woven fabric (0.92 kg $m^{-2}h^{-1}$), HK@NF (0.99 kg $m^{-2}h^{-1}$), and HB@NF (1.64 kg $m^{-2}h^{-1}$), as shown in Figure 7a. The water transportation network formed by the assembled micro-pores facilitates rapid and continuous water supply to

the upper surface, enabling efficient vapor escape and effective temperature distribution. Simultaneously, the internal structure of HB fabric enables sufficient light penetration to provide effective energy absorption and heat conversion. In order to evaluate the evaporation efficiency, cyclic stability, and endurance of HB@NF, a series of evaporation experiments were conducted under 1 kWm^{-2} and 3.2% NaCl simulated seawater. The resulting curves of the evaporation rates over five operating cycles are shown in Figure 7b.

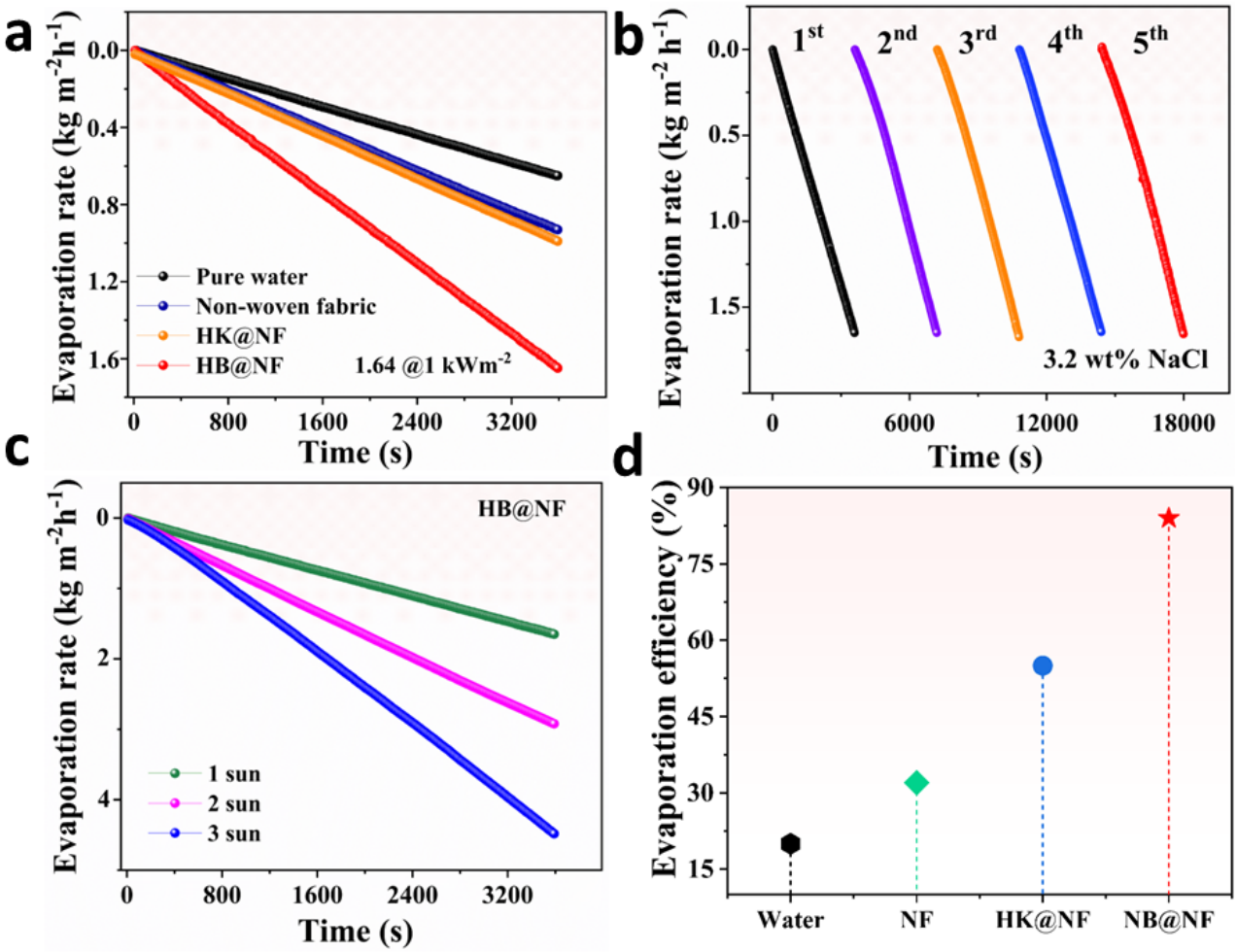

Figure 7. (**a**) Evaporation rate measurement of the four developed systems. (**b**) Evaporation rate evaluation of HB@NF hybrid solar evaporator over multiple operating cycles under 3.2 wt% NaCl condition. (**c**) Evaporation rates of HB@NF under 1, 2, 3 kWm^{-2} solar intensities. (**d**) Comparative evaporation efficiency analysis of the designed systems.

The HB@NF evaporator exhibits a consistent evaporation rate, exhibiting minimal variations in slope throughout its operation. This indicates the exceptional stability and long-lasting durability of the created system when used in continuous operation. The HB@NF evaporator has consistent evaporation rates, exhibiting little changes in slope throughout the course of operation. This indicates a high level of stability and long-lasting durability for the created system during continuous use. The HB@NF solar evaporator was further tested at different solar intensities to assess its evaporation capacity under increased solar irradiation, as seen in Figure 7c. The HB@NF solar evaporator demonstrates an evaporation rate of up to 4.48 kg $m^{-2}h^{-1}$ when subjected to solar intensity levels below 3 kWm^{-2}. This observation suggests that the evaporator exhibits an improved photothermal response when exposed to greater incident light conditions.

The corresponding photothermal conversion efficiency (η_{evap}) of the HB@NF was measured by the following equation [20,30,31]

$$\eta_{evap} = \frac{\dot{m}_v h_{LV}}{q_i} \tag{3}$$

$$h_{LV} = \Lambda + C\Delta T \tag{4}$$

where $\dot{m}_v$ corresponds to the evaporation rate (1.64 kg m^{-2} h^{-1}) after eliminating the dark evaporation rate of water, h_{LV} is the phase change enthalpy from liquid to vapor phase transition, and q_{solar} is the incident solar irradiation (1 kW m^{-2}). Λ is the latent heat while vapors are generating (energy needed for liquid–vapor phase transition), C is the specific heat capacity of water (4.2 kJ kg^{-1} K^{-1}), and ΔT is the water temperature rise under 1 kWm^{-2} from the initial state to the evaporation point. The investigations were carried out in a controlled environment with an atmospheric temperature of 28 1 °C and a relative humidity of 45%. Based on Equations (3) and (4), the calculation of HB@NF was conducted to determine the evaporation efficiency, up to a photothermal conversion efficiency of 84%, while ignoring optical and heat losses. The calculated efficiency of HB@NF (84%) surpasses that of pure water (20%), NF (32%), HK@NF (55%), and HB@NF (84%), as seen in Figure 7d. Furthermore, Table 1 represents the comparative analysis of our present research with previously published solar evaporation systems, manifesting that our system achieved the highest evaporation rate among all. The aforementioned demonstration of the HB@NF solar evaporator's performance highlights its significant potential for efficient evaporation performance and photothermal conversion, suggesting its viability as a prospective option for large-scale implementation in industrial freshwater production.

The management ability of the HB@NF-based evaporator was analyzed during the continuous water desalination under 1 kWm^{-2} solar intensity. Time-dependent salt crystallization is observed around the center towards the edges in the form of a salt ring of HB deposited fabric under one sun irradiation when desalination performance is carried out under 21% NaCl solution. Furthermore, the accumulated salt crystallizes in concentrated form and does not dissolve back in the solution even after the solar simulator is turned off for several hours. The harvested salt around the fabric edges falls off with a gentle tapping on the surface of the evaporator proving the excellent potential of the HB@NF-based evaporator for the simultaneous freshwater production and salt collection from seawater for zero liquid discharge phenomena. The mechanism of the salt accumulation around the edges can be explained by the Marangoni effect. The microporous structure of the smoke filter allows the salty water transportation from the bulk water via capillary force to the center (at the contact point) of the HB@NF. All abbreviations are explained in Abbreviations.

The hydrophilicity of the non-woven fabric transports the salt solution toward the round edges from the center. In the meantime, the photothermal effect of the HB evaporates the water molecules from the interfacial layer. The continuous water pumping from the smoke filter replenishes the evaporated water which sweeps away concentrated saline towards the edges. As the concentration of the salt gradually increases with the evaporation of water and reaches the solubility limit, the salt starts crystallizing around the edges leaving the center of HB@NF for smooth evaporation. Actually, gradients of concentration of salt on the photothermal surface trigger the Marangoni effect. The presence of a surface tension gradient at the interface results in the generation of tangential shear, which induces a slip velocity. This slip velocity propels seawater from the low surface tension region towards the high surface tension region of the interface, i.e., from the center to the edge of the evaporator. This facilitates the process of evaporation by ensuring a suitable seawater flow rate. In the context of salt collection in solar evaporation systems, the governing equations for the Marangoni effect can be derived as follows [32,33]:

$$\frac{\partial C}{\partial t} = D\nabla^2 C \tag{5}$$

where C is the concentration of salt in the solution, t is time, and D is the diffusion coefficient of salt. This equation represents the conservation of mass for the salt solution on the evaporating surface.

$$\rho C_p \frac{\partial T}{\partial t} = \nabla \cdot (k \nabla T) \tag{6}$$

ρ is the density of the solution, Cp is the specific heat capacity of the solution, T is the temperature of the solution, and k is the thermal conductivity of the solution. The temperature distribution in the evaporating pool is important for understanding the Marangoni effect, as it is driven by temperature gradients.

To account for fluid flow and the Marangoni effect, we need to solve the Navier–Stokes equation, which describes the motion of the fluid. In the presence of surface tension gradients, it is modified to include the Marangoni effect term as follows:

$$\rho \left(\frac{\partial \mathrm{v}}{\partial t} + (\mathrm{v} \cdot \nabla)\mathrm{v} \right) = -\nabla P + \nabla \cdot \sigma \tag{7}$$

v is the velocity vector of the fluid and P is pressure. σ is the stress tensor, which includes the surface tension contribution due to the Marangoni effect.

The Marangoni effect introduces an additional term in the stress tensor due to surface tension gradients. This term is proportional to the concentration gradient:

$$\sigma_{\text{Marangoni}} = -\Gamma \nabla C \tag{8}$$

Γ is the Marangoni coefficient, which characterizes the strength of the Marangoni effect.

Hence, the solute gradient in the non-woven fabric-based photothermal surface induces the Marangoni effect which accelerates the water flow and contributes to continuous water evaporation along with salt collection without deteriorating the photothermal surface. Figure 8a–h shows the time-dependent performance of the HB@NF-based hybrid solar evaporator exhibiting salt crystallization from the center towards the edges of under 21% NaCl solution under 1 kWm^{-2} solar irradiation, allowing in situ salt recovery along with fresh water production. Additionally, the water pumping path also significantly impacts the salt gradient and crystallization position on the HB@NF evaporator surface. For instance, the circular edge of the smoke filter edge pumps water at the center of non-woven fabric evenly, which is then transported towards the edges leading to edge-preferential crystallization for in situ salt harvesting. The long-term stability and anti-fouling features of HB@NF were evaluated through continuous operation over multiple cycles to assess the consistency of evaporation rates. The obtained results demonstrate uniform evaporation rates with a minor discrepancy. These findings indicate that our device exhibits excellent reliability, as depicted in Figure 8i. Therefore, the developed device has the potential to be implemented on an industrial scale for practical applications. The study investigated the efficacy of an HB@NF hybrid solar evaporator for the purification potential of condensed water. The potential of nano-filtration in removing primary and heavy metal ions was assessed using Inductively Coupled Plasma–Optical Emission Spectrometry (ICP–OES). Figure 8j illustrates the concentration of primary metal ions (Na^+, K^+, Mg^{2+}, and Ca^{2+}) in both simulated water and fresh water. It is evident that the concentration of these ions is substantially decreased in the condensed water, surpassing the standards set by the World Health Organization (WHO) for drinking water. Consequently, a self-regenerating HB@NF-based solar evaporator has been successfully developed, which not only eliminates heavy metal ions without surface degradation but also holds potential for practical implementation in industrial-scale freshwater production. Water collection efficiency is one of the most important aspects of solar evaporation systems. These technologies have a wide range of implications for resource conservation, energy efficiency, sustainability, economic viability, and various applications in various sectors. Enhancing water collection efficiency can address water-related challenges and promote sustainable water management practices. Figure 9 demonstrates the real-time water collection efficiency of freshwater using our small-scale evaporation structure. For this, our HB@NF solar evaporator is covered with a

glass beaker to condense vapors, and our petri dish is placed to collect condensate. The continuous evaporation performance of the prototype collects 22 mL freshwater during 8 h under one sun illumination.

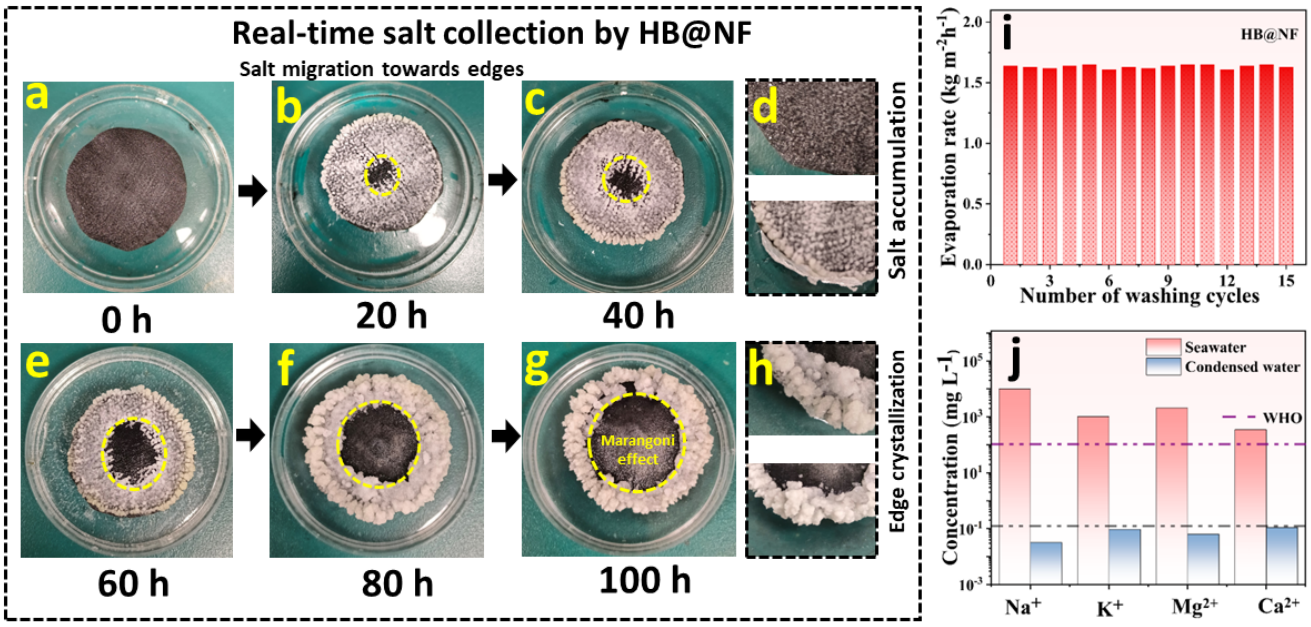

Figure 8. (**a**–**h**) Time-dependent salt transportation in the hybrid HB@NF under 1 kWm^{-2} solar evaporation: the salt migrates from the center towards the edge in the concentrated form. As saline keeps evaporating, salt becomes increasingly concentrated and accumulates at the edges. (**i**) Evaporation rates of HB@NF solar evaporator over various washing cycles. (**j**) Concentrations of primary salt ions in simulated water and condensed water when operated using HB@NF solar evaporator.

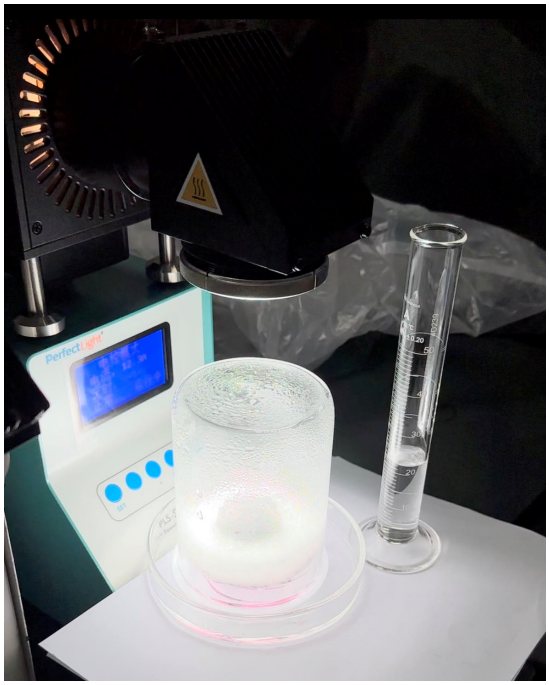

Figure 9. Small-scale prototype of freshwater collection using a glass beaker to condense vapors.

Table 1. Comparison with state-of-the-art solar evaporators.

Sr No.	Material	Absorption	Evaporation Rate	Photothermal Conversion Efficiency	Ref.
1.	Ti_2O_3	90%	1.32	92%	[34]
2.	Fe_2O_3/CNT	97%	1.42	87.2%	[35]
3.	Silk/rGO	94%	1.48	102%	[36]
4.	Polymer foams	94%	1.54	90.4%	[37]
5.	MnO_2/rGO Aerogel	100	1.35	93.8%	[38]
6.	HN/NiO	92.1	1.37	85.8%	[39]
7.	Graphene membrane	99.9	1.37	90%	[40]
8.	CuS/Sn_2S_3	92%	1.42	82.9%	[41]
9.	CuS/agaros	94%	1.63	94.9%	[42]
10.	HB@NF	96%	1.64	93%	This work

3. Conclusions

In summary, a low-cost self-regenerating hybrid solar evaporator was designed via UV-induced printing of honokiol biochar (HB) on the super hydrophilic non-woven fabric for in situ freshwater, and salt collection from seawater. The pyrolyzed biochar manifests excellent solar absorption (96%), and efficient stability in seawater. Excellent evaporation rates (1.64 kg m^{-2} h^{-1}) under 1kW m^{-2} solar irradiation are attributed to the excellent photothermal response of the HB with the excellent thermal insulation provided by the supporting matrix of polystyrene foam (PSF) and achieved efficient heat accumulation (48.5 °C) under one sun, while the centralized seawater supply via cigarette filter through the minimum contact area reduces thermal losses via conduction to the bulk water and helps to achieve the Marangoni effect for salt collection. More importantly, effective thermal activity was also validated experimentally by time-dependent IR images under 1 kWm^{-2} validation along with a model using COMSOL Multiphysics software (version 6.1) to simulate heat transfer simulation. Furthermore, a series of experimental evidence of salt collection over different periods, evaporation stability under different washing cycles, and rejection of primary metal ions via ICP-OES have been investigated. The current study provides a significant opportunity for the development of biomass-derived materials for the in situ recovery of freshwater and minerals from seawater, as potential alternatives to depleting natural resources.

Supplementary Materials: The following supporting information can be downloaded at: https://www.mdpi.com/article/10.3390/w15203697/s1. References [3,43] are cited in the supplementary materials.

Author Contributions: Conceptualization, M.A.; methodology, M.A. and M.A.A.; software, B.S.A.; validation, S.S.A. and M.A.; formal analysis, F.H.; investigation, A.A.H.; resources, M.A.; data curation, M.F.E.-T.; writing—original draft preparation, M.A.; writing—review and editing, N.A.-H. and A.A.H.; visualization, B.S.A.; supervision, M.A.; project administration, M.A.; funding acquisition, M.A. All authors have read and agreed to the published version of the manuscript.

Funding: The authors extend their appreciation to the Deputyship for Research & Innovation, Ministry of Education in Saudi Arabia for funding this research work through the project number RI-44–0202.

Data Availability Statement: Data will be provided on reasonable request from the corresponding author.

Conflicts of Interest: The authors declare no conflict of interest.

Abbreviations

Sr. No.	Name	Abbreviation
1.	Honokiol	HK
2.	honokiol biochar	HB
3.	non-woven fabric	NF
4.	Negative Emission Technologies	NET
5.	Polystyrene foam	(PSF)
6.	World Health Organization	(WHO)
7.	Inductively Coupled Plasma-Optical Emission Spectrometry	(ICP-OES)
8.	Sodium Chloride	NaCl
9.	Infrared	(IR)
10.	X-ray photoelectron spectroscopy	(XPS)
11.	Fourier transform infrared spectroscopy	(FTIR).
12.	1 sun	1 kW m^{-2}

References

1. Seckler, D.; Barker, R.; Amarasinghe, U. Water Scarcity in the Twenty-First Century. *Int. J. Water Resour. Dev.* **1999**, *15*, 29–42. [CrossRef]
2. Mekonnen, M.M.; Hoekstra, A.Y. Four Billion People Facing Severe Water Scarcity. *Sci. Adv.* **2016**, *2*, e1500323. [CrossRef] [PubMed]
3. Khawaji, A.D.; Kutubkhanah, I.K.; Wie, J.-M. Advances in Seawater Desalination Technologies. *Desalination* **2008**, *221*, 47–69. [CrossRef]
4. Ahmed, F.E.; Hashaikeh, R.; Hilal, N. Solar Powered Desalination—Technology, Energy and Future Outlook. *Desalination* **2019**, *453*, 54–76. [CrossRef]
5. Li, C.; Goswami, Y.; Stefanakos, E. Solar Assisted Sea Water Desalination: A Review. *Renew. Sustain. Energy Rev.* **2013**, *19*, 136–163. [CrossRef]
6. Wang, S.; Liu, Y.; Yang, A.; Zhu, Q.; Sun, H.; Sun, P.; Yao, B.; Zang, Y.; Du, X.; Dong, L. Xanthate-Modified Magnetic Fe_3O_4@SiO_2-Based Polyvinyl Alcohol/Chitosan Composite Material for Efficient Removal of Heavy Metal Ions from Water. *Polymers* **2022**, *14*, 1107. [CrossRef]
7. Irshad, M.S.; Wang, X.; Abbasi, M.S.; Arshad, N.; Chen, Z.; Guo, Z.; Yu, L.; Qian, J.; You, J.; Mei, T. Semiconductive, Flexible MnO2 NWs/Chitosan Hydrogels for Efficient Solar Steam Generation. *ACS Sustain. Chem. Eng.* **2021**, *9*, 3887–3900. [CrossRef]
8. Irshad, M.S.; Wang, X.; Abbas, A.; Yu, F.; Li, J.; Wang, J.; Mei, T.; Qian, J.; Wu, S.; Javed, M.Q. Salt-Resistant Carbon Dots Modified Solar Steam System Enhanced by Chemical Advection. *Carbon* **2021**, *176*, 313–326. [CrossRef]
9. Yang, Z.; Li, D.; Yang, K.; Chen, L.; Wang, J.; Zhu, X.; Chen, B. Optimized Water Supply in a Solar Evaporator for Simultaneous Freshwater Production and Salt Recycle. *Environ. Sci. Technol.* **2023**, *57*, 13047–13055. [CrossRef]
10. Zhao, W.; Gong, H.; Song, Y.; Li, B.; Xu, N.; Min, X.; Liu, G.; Zhu, B.; Zhou, L.; Zhang, X.-X.; et al. Hierarchically Designed Salt-Resistant Solar Evaporator Based on Donnan Effect for Stable and High-Performance Brine Treatment. *Adv. Funct. Mater.* **2021**, *31*, 2100025. [CrossRef]
11. Chen, C.; Zhou, L.; Yu, J.; Wang, Y.; Nie, S.; Zhu, S.; Zhu, J. Dual Functional Asymmetric Plasmonic Structures for Solar Water Purification and Pollution Detection. *Nano Energy* **2018**, *51*, 451–456. [CrossRef]
12. Irshad, M.S.; Arshad, N.; Zhang, J.; Song, C.; Mushtaq, N.; Alomar, M.; Shamim, T.; Dao, V.-D.; Wang, H.; Wang, X.; et al. Wormlike Perovskite Oxide Coupled with Phase-Change Material for All-Weather Solar Evaporation and Thermal Storage Applications. *Adv. Energy Sustain. Res.* **2023**, *4*, 2200158. [CrossRef]
13. Irshad, M.S.; Wang, X.; Arshad, N.; Javed, M.Q.; Shamim, T.; Guo, Z.; Li, H.R.; Wang, J.; Mei, T. Bifunctional In-Situ Polymerized Nanocomposites for Convective Solar Desalination and Enhanced Photo-Thermoelectric Power Generation. *Environ. Sci. Nano* **2022**, *9*, 1685–1698. [CrossRef]
14. Wang, J.; Shamim, T.; Arshad, N.; Irshad, M.S.; Mushtaq, M.N.; Zhang, C.; Yousaf, M.; Alshahrani, L.A.; Akbar, M.; Lu, Y. In Situ Polymerized Fe2O3@ PPy/Chitosan Hydrogels as a Hydratable Skeleton for Solar-Driven Evaporation. *J. Am. Ceram. Soc.* **2022**, *105*, 5325–5335. [CrossRef]
15. Fuzil, N.S.; Othman, N.H.; Alias, N.H.; Marpani, F.; Othman, M.H.D.; Ismail, A.F.; Lau, W.J.; Li, K.; Kusworo, T.D.; Ichinose, I.; et al. A Review on Photothermal Material and Its Usage in the Development of Photothermal Membrane for Sustainable Clean Water Production. *Desalination* **2021**, *517*, 115259. [CrossRef]
16. Lin, Y.; Xu, H.; Shan, X.; Di, Y.; Zhao, A.; Hu, Y.; Gan, Z. Solar Steam Generation Based on the Photothermal Effect: From Designs to Applications, and Beyond. *J. Mater. Chem. A* **2019**, *7*, 19203–19227. [CrossRef]
17. Tan, K.W.; Yap, C.M.; Zheng, Z.; Haw, C.Y.; Khiew, P.S.; Chiu, W.S. State-of-the-Art Advances, Development, and Challenges of Metal Oxide Semiconductor Nanomaterials for Photothermal Solar Steam Generation. *Adv. Sustain. Syst.* **2022**, *6*, 2100416. [CrossRef]

18. Dao, V.-D.; Vu, N.H.; Yun, S. Recent Advances and Challenges for Solar-Driven Water Evaporation System toward Applications. *Nano Energy* **2020**, *68*, 104324. [CrossRef]
19. Ding, T.; Zhou, Y.; Ong, W.L.; Ho, G.W. Hybrid Solar-Driven Interfacial Evaporation Systems: Beyond Water Production towards High Solar Energy Utilization. *Mater. Today* **2021**, *42*, 178–191. [CrossRef]
20. Irshad, M.S.; Arshad, N.; Liu, G.; Mushtaq, N.; Lashari, A.A.; Qin, W.; Asghar, M.S.; Li, H.; Wang, X. Biomass-Printed Hybrid Solar Evaporator Derived from Bio-Polluted Invasive Species, a Potential Step toward Carbon Neutrality. *ACS Appl. Mater. Interfaces* **2023**, *15*, 16607–16620. [CrossRef]
21. Yu, F.; Guo, Z.; Xu, Y.; Chen, Z.; Irshad, M.S.; Qian, J.; Mei, T.; Wang, X. Biomass-Derived Bilayer Solar Evaporator with Enhanced Energy Utilization for High-Efficiency Water Generation. *ACS Appl. Mater. Interfaces* **2020**, *12*, 57155–57164. [CrossRef] [PubMed]
22. Lonappan, L.; Rouissi, T.; Das, R.K.; Brar, S.K.; Ramirez, A.A.; Verma, M.; Surampalli, R.Y.; Valero, J.R. Adsorption of Methylene Blue on Biochar Microparticles Derived from Different Waste Materials. *Waste Manag.* **2016**, *49*, 537–544. [CrossRef]
23. Munroe, M.E.; Arbiser, J.L.; Bishop, G.A. Honokiol, a Natural Plant Product, Inhibits Inflammatory Signals and Alleviates Inflammatory Arthritis. *J. Immunol.* **2007**, *179*, 753–763. [CrossRef] [PubMed]
24. Shen, J.-L.; Man, K.-M.; Huang, P.-H.; Chen, W.-C.; Chen, D.-C.; Cheng, Y.-W.; Liu, P.-L.; Chou, M.-C.; Chen, Y.-H. Honokiol and Magnolol as Multifunctional Antioxidative Molecules for Dermatologic Disorders. *Molecules* **2010**, *15*, 6452–6465. [CrossRef] [PubMed]
25. Crane, C.; Panner, A.; Pieper, R.O.; Arbiser, J.; Parsa, A.T. Honokiol Mediated Inhibition of PI3K/MTOR Pathway: A Potential Strategy to Overcome Immunoresistance in Glioma, Breast and Prostate Carcinoma without Impacting T Cell Function. *J. Immunother.* **2009**, *32*, 585. [CrossRef] [PubMed]
26. Jiang, Y.; An, N.; Sun, Q.; Guo, B.; Wang, Z.; Zhou, W.; Gao, B.; Li, Q. Biomass Hydrogels Combined with Carbon Nanotubes for Water Purification via Efficient and Continuous Solar-Driven Steam Generation. *Sci. Total Environ.* **2022**, *837*, 155757. [CrossRef]
27. Yang, L.; Li, N.; Guo, C.; He, J.; Wang, S.; Qiao, L.; Li, F.; Yu, L.; Wang, M.; Xu, X. Marine Biomass-Derived Composite Aerogels for Efficient and Durable Solar-Driven Interfacial Evaporation and Desalination. *Chem. Eng. J.* **2020**, *417*, 128051. [CrossRef]
28. Chen, X.; Wu, Z.; Lai, D.; Zheng, M.; Xu, L.; Huo, J.; Chen, Z.; Yuan, B.; Fu, M.-L. Resilient Biomass-Derived Hydrogel with Tailored Topography for Highly Efficient and Long-Term Solar Evaporation of High-Salinity Brine. *J. Mater. Chem. A* **2020**, *8*, 22645–22656. [CrossRef]
29. Lin, X.; Wang, P.; Hong, R.; Zhu, X.; Liu, Y.; Pan, X.; Qiu, X.; Qin, Y. Fully Lignocellulosic Biomass-Based Double-Layered Porous Hydrogel for Efficient Solar Steam Generation. *Adv. Funct. Mater.* **2022**, *32*, 2209262. [CrossRef]
30. Zhu, M.; Xia, A.; Feng, Q.; Wu, X.; Zhang, C.; Wu, D.; Zhu, H. Biomass Carbon Materials for Efficient Solar Steam Generation Prepared from Carbonized Enteromorpha Prolifera. *Energy Technol.* **2020**, *8*, 1901215. [CrossRef]
31. Lei, Z.; Sun, X.; Zhu, S.; Dong, K.; Liu, X.; Wang, L.; Zhang, X.; Qu, L.; Zhang, X. Nature Inspired MXene-Decorated 3D Honeycomb-Fabric Architectures Toward Efficient Water Desalination and Salt Harvesting. *Nano-Micro Lett.* **2022**, *14*, 10. [CrossRef] [PubMed]
32. Zhang, L.; Li, X.; Zhong, Y.; Leroy, A.; Xu, Z.; Zhao, L.; Wang, E.N. Highly Efficient and Salt Rejecting Solar Evaporation via a Wick-Free Confined Water Layer. *Nat. Commun.* **2022**, *13*, 849. [CrossRef] [PubMed]
33. Chen, Y.; Yang, J.; Zhu, L.; Wang, S.; Jia, X.; Li, Y.; Shao, D.; Feng, L.; Song, H. Marangoni-Driven Biomimetic Salt Secretion Evaporator. *Desalination* **2023**, *548*, 116287. [CrossRef]
34. Tao, F.; Zhang, Y.; Yin, K.; Cao, S.; Chang, X.; Lei, Y.; Wang, D.; Fan, R.; Dong, L.; Yin, Y.; et al. Copper Sulfide-Based Plasmonic Photothermal Membrane for High-Efficiency Solar Vapor Generation. *ACS Appl. Mater. Interfaces* **2018**, *10*, 35154–35163. [CrossRef]
35. Li, W.; Li, X.; Liu, J.; Zeng, M.; Feng, X.; Jia, X.; Yu, Z.-Z. Coating of Wood with Fe2O3-Decorated Carbon Nanotubes by One-Step Combustion for Efficient Solar Steam Generation. *ACS Appl. Mater. Interfaces* **2021**, *13*, 22845–22854. [CrossRef]
36. Ni, F.; Xiao, P.; Qiu, N.; Zhang, C.; Liang, Y.; Gu, J.; Xia, J.; Zeng, Z.; Wang, L.; Xue, Q.; et al. Collective Behaviors Mediated Multifunctional Black Sand Aggregate towards Environmentally Adaptive Solar-to-Thermal Purified Water Harvesting. *Nano Energy* **2020**, *68*, 104311. [CrossRef]
37. Zhang, Z.; Mu, P.; Han, J.; He, J.; Zhu, Z.; Sun, H.; Liang, W.; Li, A. Superwetting and Mechanically Robust MnO_2 Nanowire–Reduced Graphene Oxide Monolithic Aerogels for Efficient Solar Vapor Generation. *J. Mater. Chem. A* **2019**, *7*, 18092–18099. [CrossRef]
38. Li, G.; Law, W.-C.; Chan, K.C. Floating, Highly Efficient, and Scalable Graphene Membranes for Seawater Desalination Using Solar Energy. *Green Chem.* **2018**, *20*, 3689–3695. [CrossRef]
39. Qin, D.-D.; Zhu, Y.-J.; Yang, R.-L.; Xiong, Z.-C. A Salt-Resistant Janus Evaporator Assembled from Ultralong Hydroxyapatite Nanowires and Nickel Oxide for Efficient and Recyclable Solar Desalination. *Nanoscale* **2020**, *12*, 6717–6728. [CrossRef]
40. Li, C.; Jiang, D.; Huo, B.; Ding, M.; Huang, C.; Jia, D.; Li, H.; Liu, C.-Y.; Liu, J. Scalable and Robust Bilayer Polymer Foams for Highly Efficient and Stable Solar Desalination. *Nano Energy* **2019**, *60*, 841–849. [CrossRef]
41. Ibrahim, I.; Seo, D.H.; Angeloski, A.; McDonagh, A.; Shon, H.K.; Tijing, L.D. 3D Microflowers CuS/Sn_2S_3 Heterostructure for Highly Efficient Solar Steam Generation and Water Purification. *Sol. Energy Mater. Sol. Cells* **2021**, *232*, 111377. [CrossRef]

42. Wu, X.; Robson, M.E.; Phelps, J.L.; Tan, J.S.; Shao, B.; Owens, G.; Xu, H. A Flexible Photothermal Cotton-CuS Nanocage-Agarose Aerogel towards Portable Solar Steam Generation. *Nano Energy* **2019**, *56*, 708–715. [CrossRef]
43. Saleque, A.M.; Saha, S.; Ivan MN, A.S.; Ahmed, S.; Alam, T.I.; Hani, S.U.; Tsang, Y.H. Reduced graphene oxide/$TiTe_2$ quantum dot coated waste face mask recycled for highly efficient solar steam generation. *Sol. Energy Mater. Sol. Cells* **2023**, *253*, 112232. [CrossRef]